Nanoscale RSC Publishing

COMMUNICATION

Cite this: DOI: 10.1039/x0xx00000x

Highly active and durable platinum-lead bimetallic alloy nanoflowers for formic acid electrooxidation†

Mingxing Gong,[b§] Fumin Li,[a§] Zhigang Yao,[b] Suqi Zhang,[b] Jingwen Dong,[b] Yu Chen,[*a] and Yawen Tang[b]

Received 00th January 2012,
Accepted 00th January 2012

DOI: 10.1039/x0xx00000x

www.rsc.org/

The $Pt_{84}Pb_{16}$ (atomic ratio) bimetallic alloy nanoflowers ($Pt_{84}Pb_{16}$ BANFs) are synthesized by a simple one-pot hydrothermal reduction method, which effectively enhance the dehydrogenation pathway of the formic acid oxidation reaction (FAOR) due to ensemble effect and electronic effect. As a result, the mass activity of $Pt_{84}Pb_{16}$ BANFs for the FAOR is 16.7 times higher than that of commercial Pt black at 0.3 V potential.

Direct formic acid fuel cells (DFAFCs), a clean and green energy conversion device, has attracted increased attention in recent years due to its outstanding advantages, such as low formic acid crossover, high theoretical open circuit voltage, and facile power-system integration.[1, 2] Over the past four decades, the formic acid oxidation reaction (FAOR) on both Pt and Pd electrocatalysts has been investigated intensively. It is generally accepted that the FAOR on the Pt and Pd surface obeys a dual-path mechanism in acidic electrolyte.[3, 4] Dehydrogenation (direct pathway) produces CO_2, while dehydration (indirect pathway) produces poisoning intermediate CO_{ads}. Compared to Pt electrocatalyst, Pd electrocatalyst is more active for the FAOR due to the preferential dehydrogenation pathway on the Pd surface, but is less stable due to the dissolution of Pd metal in the corrosive formic acid solution.[5] In contrast, Pt electrocatalyst has excellent electrochemical stability due to the excellent chemical inertness of Pt metal, but has low electrocatalytic activity for the FAOR due to the predominant dehydration pathway at low potential, which results in inactivity of pure Pt electrocatalyst due to the CO_{ads} poisoning.

Based on ensemble effect and/or electronic effect, modifying Pt with foreign metals[6-10] or alloying Pt with other metals[11-13] can remarkably facilitate the dehydrogenation pathway of the FAOR on the Pt surface, and consequently enhance the activity and durability of Pt-based electrocatalysts for the FAOR. Among Pt-based multimetallic electrocatalysts with controllable composition (such as PtAu, PtNi, PtCu, PtCo, PtMn, and PtPb, etc.),[5, 11-30] PtPb bimetallic nanocrystals is one of the most promising candidates due to high CO_{ads} tolerance, excellent catalytic activity, and abundant source of lead.[11, 14-18, 31-33]

Apart from the chemical composition regulation, the electrocatalytic activity and durability of Pt-based electrocatalysts can also be improved by controlling their morphologies. In this regard, Pt-based nanoflowers with branched structure generally display the improved electrocatalytic activity and durability for many important electrochemical reactions, such as FAOR,[34, 35] methanol oxidation reaction,[36, 37] and oxygen reduction reaction,[38, 39] *etc*. On the one hand, the big surface area, effective mass transfer, excellent electrical connectivity, and high density of twinned defects contribute to the improvement in electrocatalytic activity of nanoflowers. On the other hand, the three-dimensionally interconnected structure of nanoflowers effectively restrains Ostwald ripening and growth of every nanocrystal building block, and consequently improves their durability.[34-39] Till now, the solution phase synthesis of Pt-based nanoflowers with branched structure is still a challenging because face-centered cubic (*fcc*) precious metals have no intrinsic driving force for the growth of anisotropic structures due to inherently highly symmetric fcc crystal lattice.[40-42]

In the present work, we demonstrated an effective one-step hydrothermal co-reduction route to synthesize $Pt_{84}Pb_{16}$ (atomic ratio) bimetallic alloy nanoflowers (BANFs). The as-prepared $Pt_{84}Pb_{16}$ BANFs effectively hindered the dehydration pathway of the FAOR, and consequently showed superior electrocatalytic activity and durability for the FAOR compared to commercial Pt black.

In a typical synthesis, $Pt_{84}Pb_{16}$ BANFs was readily obtained by heating mixture solution of K_2PtCl_4, $Pb(NO_3)_2$, polyallylamine hydrochloride (PAH, Scheme S1 in ESI†) and HCHO at 120 ^{o}C for 6 h (see the Supporting Information for experimental details). The chemical composition and crystal structure of the products were first investigated by energy dispersive X-ray (EDX), Leeman inductively coupled plasma atomic emission spectrometry (ICP-AES), and X-ray diffraction (XRD) techniques. EDX analysis indicates that the products are composed of Pt and Pb elements, and the approximate Pt/Pb atomic ratio is 84:16 (Fig. 1A), which is very close to ICP-AES result (86:14) but much lower than the initial Pt^{II}/Pb^{II} adding ratio (1:2) in reaction system. XRD pattern of $Pt_{84}Pb_{16}$ nanocrystals shows four diffraction peaks at 39.52, 46.01, 67.29, 80.87 (Fig. 1B), corresponding to the {111}, {200}, {220}, and {311} facets of the *fcc* Pt. Compared to Pt black, the four diffraction peaks of $Pt_{84}Pb_{16}$ nanocrystals shift to lower angles. And, no any diffraction peaks of metallic Pb or Pb oxides/hydroxides are observed. Thus, XRD results clearly demonstrate that $Pt_{84}Pb_{16}$ nanocrystals are alloy.[11, 32] According to the Vegard's law, the lattice constant (a) of $Pt_{84}Pb_{16}$ nanocrystals is 0.4062 nm, bigger than that of Pt black (a=0.3922 nm), reflecting the lattice expansion due to the partial replacement of Pt atoms by Pb atoms with a larger atom radius (Pt: 1.39 Å vs. Pb: 1.75 Å). The average particle size of $Pt_{84}Pb_{16}$ nanocrystals is calculated from the {111} diffraction peak to be ca. 6 nm, using the Scherrer formula.

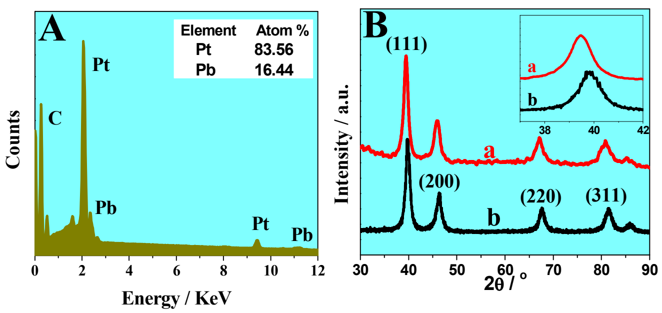

Fig. 1 (A) EDX spectrum of $Pt_{84}Pb_{16}$ nanocrystals. (B) XRD patterns of (a) $Pt_{84}Pb_{16}$ nanocrystals and (b) commercial Pt black.

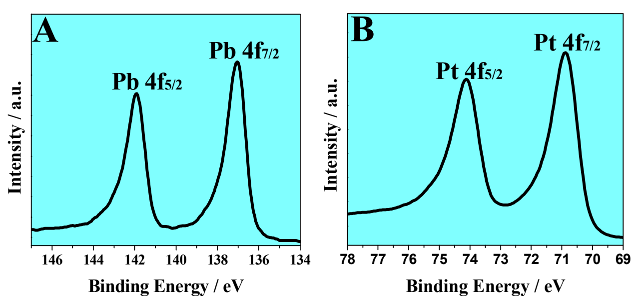

Fig. 2 (A) Pb 4f and (B) Pt 4f XPS spectra of $Pt_{84}Pb_{16}$ nanocrystals.

The surface composition and electronic property of $Pt_{84}Pb_{16}$ nanocrystals were examined by X-ray photoelectron spectroscopy (XPS). XPS measurement indicates the surface atom composition of $Pt_{84}Pb_{16}$ nanocrystals is $Pt_{73}Pb_{27}$ (Fig. S1 in ESI†). The surface enrichment of Pb on the surface of $Pt_{84}Pb_{16}$ nanocrystals may originate from the delayed reduction of Pb^{II} precursor due to it lower reduction potential compared to Pt^{II} precursor ($\varphi PtCl_4^{2-}/Pt$=0.755 V; $\varphi Pb^{2+}/Pb$=–0.126 V vs. NHE). The binding energies of Pb $4f_{5/2}$ and Pb $4f_{7/2}$ locate at 142.1 and 137.2 eV, corresponding to metallic Pb (Fig. 2A).[15, 16, 31] The binding energies of Pt $4f_{5/2}$ and Pt $4f_{7/2}$ are observed at 74.1 and 70.9 eV, respectively, which is indicative of metallic Pt (Fig. 2B). Compared to the standard Pt 4f binding energy value of bulk Pt (Pt $4f_{5/2}$: 74.5 eV; Pt $4f_{7/2}$: 71.2 eV[43]), Pt 4f binding energy in $Pt_{84}Pb_{16}$ nanocrystals is negatively shifted by 0.3 eV, suggesting that the electronic property of Pt atoms in $Pt_{84}Pb_{16}$ nanocrystals is changed due to the doping of the Pb element and the lattice expansion.[16]

Physical features of the products were examined by scanning electron microscopy (SEM) and transmission electron microscopy (TEM). SEM image clearly reveals that $Pt_{84}Pb_{16}$ nanocrystals have a rough surface (Fig. 3A). Low-resolution TEM image shows the average diameter of $Pt_{84}Pb_{16}$ nanocrystals is ca. 80 nm (Fig. 3B). Middle-resolution TEM image shows $Pt_{84}Pb_{16}$ nanocrystals have flower-like morphology, containing several subunits (Fig. 3C). And, the diameter of grains as building subunits is ~7 nm (Fig. 3C), in consistent with XRD data. Selected-area electron diffraction (SAED) image displays an irregularly dotted pattern (Fig. 3D), revealing their polycrystalline structure. The high resolution TEM (HRTEM) image shows that the interplanar spacing of $Pt_{84}Pb_{16}$ nanocrystals is ca. 0.232 nm (Fig. 3E), slightly bigger than {111} crystal plane of the fcc Pt (0.226 nm), originating from the lattice expansion due to the formation of PtPb alloy. The corresponding fast Fourier transform (FFT) pattern show six-fold symmetry point, further confirming the {111} crystal plane. The structure characteristic of $Pt_{84}Pb_{16}$ nanocrystals were determined by high-angle annular dark-field scanning TEM (HAADF-STEM) technique. The element mapping images reveal that both Pt and Pb elements have the homogeneous distribution in each nanoflower, and the profiles are almost same, confirming the formation of the Pt-Pb alloy (Fig. 3F).

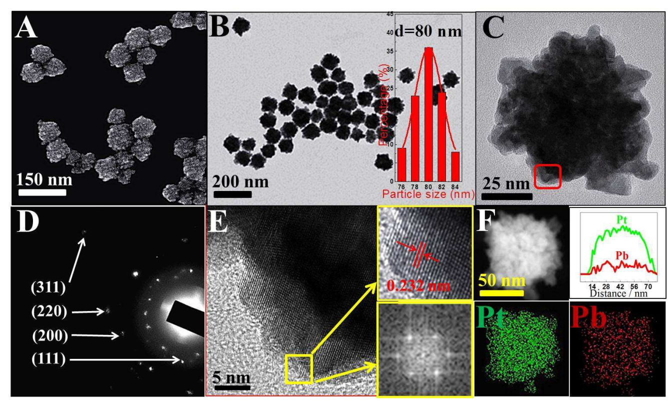

Fig. 3 (A) SEM, (B) low-resolution, and (C) middle-resolution TEM images of $Pt_{84}Pb_{16}$ BANFs. Insert in Fig. B is the size distribution histogram of $Pt_{84}Pb_{16}$ BANFs. (D) SAED image of $Pt_{84}Pb_{16}$ BANFs. (E) The HRTEM image recorded from region marked by squares in Fig. C and corresponding FFT pattern. (F) High-angle annular dark-field scanning TEM and EDX mapping images of Pt and Pb elements.

During the synthesis of $Pt_{84}Pb_{16}$ BANFs, PAH plays an important role. In the absence of PAH, the products are made up of non-dispersed bulky aggregates (Fig. S2A in ESI†), indicating that PAH can effectively act as capping agent due to its excellent hydrophily and big molecule size.[37, 44-46] In the presence of the small amount of PAH (i.e., 0.2 ml of 0.5 M PAH), the monodispersed PtPb nanocrystals are obtained (Fig. S2B in ESI†). As well known, the slow reduction rate of the precursor is crucial for the kinetically controlled synthesis of metal nanocrystals. A small amount of PAH is not enough to generate PAH-Pt^{II} and PAH-Pb^{II} complexes with slow reduction rate.[46] Thus, PAH mainly act as capping agent to facilitate the generation of monodispersed PtPb nanocrystals during the thermodynamically controlled synthesis. When increasing the amount of PAH from 2.0 mL to 4.0 mL, PtPb nanoflowers also are obtained (Fig. S2C in ESI†), which is very similar to the morphology of $Pt_{84}Pb_{16}$ BANFs in Fig. 3.

Meanwhile, it is observed that single $Pb(NO_3)_2$ precursor can't be reduced by HCHO to generate Pb nanocrystals at 120 °C for 6 h. It is well know that the underpotential deposition of Pb on Pt surface generally occurs, which elevates the Nernst equilibrium potential of Pb^{II}/Pb couple. Consequently, the PtPb alloy nanocrystals can be achieved by the catalytic reduction of Pb^{II} ion by Pt crystal nuclei and the interdiffusion process between Pb and Pt atoms at high temperature, similar to cases of Pt-Cu[37] and Pt-Ni[47] alloy nanocrystals. Meanwhile, it is observed that the molar ratio of K_2PtCl_4 to $Pb(NO_3)_2$ determines the morphology and size of the products. When decreasing the molar ratio of K_2PtCl_4 to $Pb(NO_3)_2$, the surface roughness of the resultant product gradually increases. Specifically, the resultant products evolve from Pt nanocubes (Fig. 4A) to PdPb nanoflowers (Fig. 4E) with decreasing the molar ratio of K_2PtCl_4 to $Pb(NO_3)_2$ from 1:0 to 1:2, accompanying with increasing the particle size of nanocrystals from 15 to 80 nm. Further decreasing the molar ratio of K_2PtCl_4 to $Pb(NO_3)_2$ to 1:4, the resultant PtPb nanocrystals generate the severe aggregation (Fig. 4F).

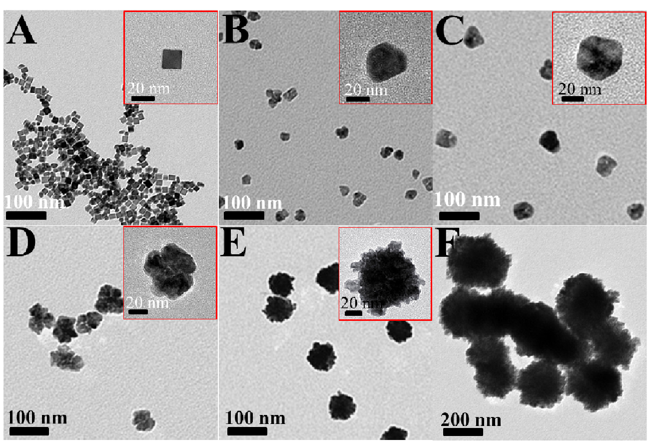

Fig. 4 (A) TEM images of the products synthesized at different molar ratio of K_2PtCl_4 to $Pb(NO_3)_2$ (A) 1:0, (B) 4:1, (C) 2:1, (D) 1:1, (E) 1:2, and (F) 1:4. In the reaction system, the concentration of K_2PtCl_4 is constant.

Due to the lower Nernst equilibrium potential of Pb^{II}/Pb couple compare to than that of O_2/H_2O couple ($\varphi Pb^{2+}/Pb$ = –0.126 V; $\varphi O_2/H_2O$=1.23 V vs. NHE), Pb atoms on PtPb alloy nanocrystals can be oxidized by O_2 in the air. Meanwhile, PAH easily coordinate to Pb^{II} species to generate the water-soluble PAH-Pb^{II} complex due to its excellent coordination ability (Fig. S3 in ESI†), resulting in the partial removal of the Pb atoms on PtPb alloy nanocrystals. Indeed, the black Pb nanocrystals prepared by $NaBH_4$ reduction can completely change to the colorless PAH-Pb^{II} complex solution in the presence of the air under the continuous string conditions (Fig. S4 in ESI†). Thus, PAH-assisted oxidation-dissolution is responsible for the lower Pt/Pb atomic ratio of PtPb alloy nanocrystals compared to initial Pt^{II}/Pb^{II} adding ratio in reaction system. During the removal of Pb atoms, the Pt^{II} and Pb^{II} precursors in reaction solution still continuously are reduced by HCHO. However, the deposited Pb atoms have higher susceptibility and dissolution rate compared to Pt atoms. The continuous deposition/partial-dissolution process results in the formation of PtPb alloy nanoflowers, as shown in Scheme 1. As shown in Fig. 4, Pt nanocubes evolve into PdPb nanoflowers (i.e., surface roughness increase) with increasing the concentration of Pb^{II} precursor during the synthesis, which in turn confirm the mentioned continuous deposition/partial-dissolution mechanism. Specifically, the higher Pb^{II} precursor concentration results in the stronger deposition/dissolution process, and consequently generate the rougher surface (i.e., the evolvement from Pt nanocubes to PdPb nanoflowers).

The electrochemically surface areas (ECSA) of $Pt_{84}Pb_{16}$ BANFs and Pt black are determined by cyclic voltammetry in a N_2-saturated 0.5 M H_2SO_4 solution. According to hydrogen adsorption charge, ECSA of $Pt_{84}Pb_{16}$ BANFs and Pt black is estimated to be 15.3 $m^2\,g_{Pt}^{-1}$ and 17.8 $m^2\,g_{Pt}^{-1}$, respectively (Fig. 5A). The smaller ECSA value of $Pt_{84}Pb_{16}$ BANFs originates from the bigger particle size of $Pt_{84}Pb_{16}$ BANFs (80 nm) compared to commercial Pt black (8.7 nm[48]).

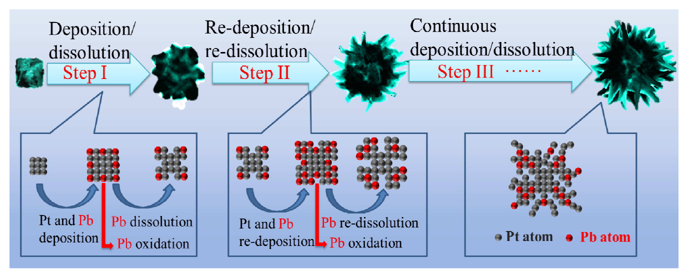

Scheme 1. Formation Mechanism of $Pt_{84}Pb_{16}$ BANFs.

Electrocatalytic activity of $Pt_{84}Pb_{16}$ BANFs and Pt black for the FAOR were evaluated by cyclic voltammetry tests in a N_2-saturated 0.5 M H_2SO_4 containing 0.5 M HCOOH solutions using the same ECSA value (Fig. 5B). The peak I at 0.54 V vs. NHE and peak II at 0.94 V vs. NHE at Pt black correspond to the oxidation of formic acid via the dehydrogenation pathway and dehydration pathway, respectively.[19] The ratio between peak I and peak II, which is defined as pathway factor R, is used to investigate the pathway of the FAOR at the electrocatalysts. R value of FAOR at $Pt_{84}Pb_{16}$ BANFs (R=5.4) is 45 times bigger than that at Pt black (R=0.12), demonstrating that the FAOR at $Pt_{84}Pb_{16}$ BANFs is achieved predominantly though the dehydrogenation pathway.

It is well known that the reaction pathway of the FAOR is highly sensitive to the actual surface structure of Pt atoms. In particular, the isolated Pt atom facilitate the dehydrogenation pathway of FAOR.[12] Upon alloying Pt with Pb, the contiguous Pt atoms are interrupted by Pb atoms to generate the isolated Pt atoms. By controlling the feed ratio of Pt^{II}/Pb^{II} precursors, various PtPb alloy nanocrystals with different Pt/Pb atomic ratio were achieved conveniently (Fig. 4, and Table S1 in ESI†). Among various PtPb alloy nanocrystals, the as-prepared $Pt_{84}Pb_{16}$ BANFs have the highest R value of FAOR (Fig. S5 in ESI†), indicating the highest electrocatalytic activity for the FAOR. Similar to other noble metal nanoflowers with the abundant defects atoms,[34-39, 49] the as-prepared $Pt_{84}Pb_{16}$ BANFs should have a large number of defects atoms (These defect atoms also belong to isolated atoms) due to the same morphology. Thus, the abundant isolated atoms make the dehydrogenation pathway dominant at $Pt_{84}Pb_{16}$ BANFs.

Apart from the ensemble effect, the electronic structure of Pt atoms also affects the reaction pathway of the FAOR. The previous investigation has indicated that the negative shift in the d-band electron center of Pt atom facilitate the dehydrogenation pathway of FAOR.[20] XPS result in Fig. 2 has demonstrated that alloying Pt with Pb results in the negative shift of Pt binding energy. Thus, the electronic modification of Pt by Pb decrease the adsorption strength of carbonaceous intermediates due to the change of d-band center of Pt, which facilities the oxidation of the intermediates, and ultimately enhances the intrinsic kinetics of FAOR.[50, 51] Furthermore, it is worth noting that the pathway factor R (5.4) of FAOR at $Pt_{84}Pb_{16}$ BANFs is much higher than that on the previously reported PtCu (ca. 0.25~0.7),[5, 13, 24-28] PtCo (ca. 0.6),[29] PtAg (ca. 0.6~2.0),[20, 52] PtNi (ca. 0.3),[21] and PtMn (ca. 0.1)[30] nanocrystals, indicating that $Pt_{84}Pb_{16}$ BANFs are highly active for the FAOR. The predominant dehydrogenation pathway results in a large enhancement in the electrocatalytic activity of Pt electrocatalysts for the FAOR at low potential. At 0.3 V vs. NHE potential, a typical anodic working voltage in DFAFC,[23, 51] the current density of FAOR on $Pt_{84}Pb_{16}$ BANFs reaches 5.01 A m^{-2}, which is about 19-fold as large as that commercial Pt black (0.26 A m^{-2}). Obviously, $Pt_{84}Pb_{16}$ BANFs has much higher electrocatalytic activity for the FAOR.

The mass activity of electrocatalysts is generally used to assess the practical applicability of electrocatalysts. Pt-mass activity of $Pt_{84}Pb_{16}$ BANFs (76.63 A g_{Pt}^{-1}) for the FAOR remain 16.7 times higher than that of and commercial Pt black (4.56 A g_{Pt}^{-1}) at 0.3 V vs. NHE potential (Fig. 5C), demonstrating the great advantage of $Pt_{84}Pb_{16}$ BANFs for Pt-saving electrocatalysts.[22]

The durability of $Pt_{84}Pb_{16}$ BANFs and Pt black for the FAOR were investigated by chronoamperommetry tests in a N_2-saturated 0.5 M H_2SO_4 containing 0.5 M HCOOH solutions at 0.5 V vs. NHE potential using the same Pt loading. At 4500 s, the currents of the FAOR on $Pt_{84}Pb_{16}$ BANFs and commercial Pt black decrease to 33.6% and 4.25% of their initial values, respectively (Fig. 5D), thus indicating that $Pt_{84}Pb_{16}$ BANFs are more stable as an electrocatalyst. Mainly, the predominant dehydrogenation pathway contributes to the enhancement in durability of $Pt_{84}Pb_{16}$ BANFs for the FAOR due to less CO_{ads} accumulation. After chronoamperometry run, no obvious morphological change occurs for $Pt_{84}Pb_{16}$ BANFs (Fig. S6 in ESI†), attributing to the 3D interconnected structure of nanoflowers.[36-39]

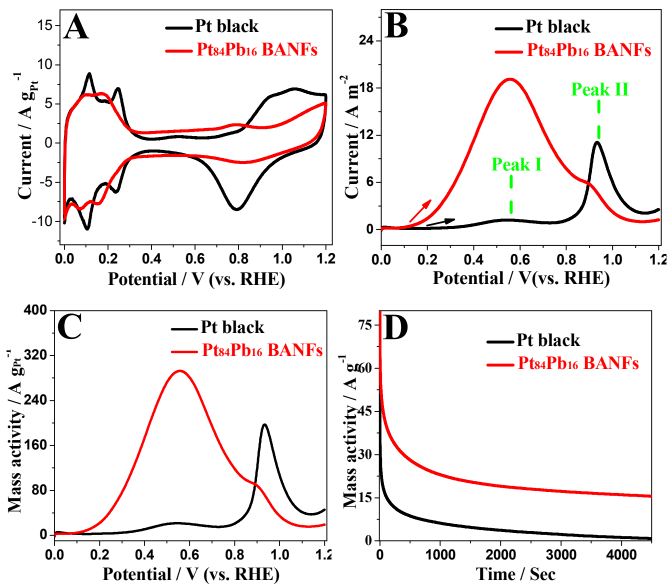

Fig. 5 (A) Cyclic voltammograms of (a) $Pt_{84}Pb_{16}$ BANFs and (b) Pt black in the N_2-saturated 0.5 M H_2SO_4 electrolyte at 50 mV s^{-1}. (B) ECSA-normalized and (C) Pt mass-normalized cyclic voltammograms of (a) $Pt_{84}Pb_{16}$ BANFs and (b) Pt black in the N_2-saturated 0.5 M HCOOH + 0.5 M H_2SO_4 solution at the scan rate of 50 mV s^{-1}. (D) Chronoamperometric curves of (a) $Pt_{84}Pb_{16}$ BANFs and (b) Pt black in the N_2-saturated 0.5 M HCOOH + 0.5 M H_2SO_4 solution at 0.5 V vs. NHE.

In summary, this work presents a successful synthesis of $Pt_{84}Pb_{16}$ BANFs via a facile one-pot hydrothermal method. The catalytic reduction of Pb^{II} on preformed Pt crystal nuclei leads to the formation of the PtPb alloy. PAH-assisted oxidation/partial-dissolution of Pb atoms and the continuous PtPb deposition/partial dissolution of Pb atoms process lead to the shape evolution from Pt nanocubes to PdPb nanoflowers. Due to geometric effect and electronic effect, $Pt_{84}Pb_{16}$ BANFs facilitate the dehydrogenation pathway of FAOR, resulting in significantly enhanced electrocatlytic activity and durability for FAOR. At 0.3 V vs. NHE potential, a typical anodic working voltage in DFAFC, the mass activity of $Pt_{84}Pb_{16}$ BANFs for the FAOR is 14.5 times higher than that of and commercial Pt black. Such superior electrocatalytic performance and chemical stability of Pt metal make $Pt_{84}Pb_{16}$ BANFs the promising anodic electrocatalysts in DFAFCs industry.

Acknowledgments

This research was sponsored by National Natural Science Foundation of China (21473111, 21376122 and 21273116), Natural Science Foundation of Jiangsu Province (BK20131395), United Fund of NSFC and Yunnan Province (U1137602), Industry-Academia Cooperation Innovation Fund Project of Jiangsu Province (BY2012001), the National Basic Research Program of China (973 Program, 2012CB215500), Fundamental Research Funds for the Central Universities (GK201402016), and a project funded by the Priority Academic Program Development of Jiangsu Higher Education Institutions.

Notes and references

[a] *School of Materials Science and Engineering, Shaanxi Normal University, Xi'an 710062, China*
E–mail: ndchenyu@gmail.com (Y. Chen)
[b] *Jiangsu Key Laboratory of New Power Batteries, Jiangsu Collaborative Innovation Center of Biomedical Functional Materials, College of Chemistry and Materials Science, Nanjing Normal University, Nanjing 210023, PR China.*
‡ These two authors made an equal contribution to this work.

† Electronic Supplementary Information (ESI) available: Experimental Details. See DOI: 10.1039/c000000x/

1. J. Chang, L. Feng, C. Liu, W. Xing and X. Hu, *Angew. Chem. Int. Edit.*, 2014, **53**, 122-126.
2 . Y. Kim, H. J. Kim, Y. S. Kim, S. M. Choi, M. H. Seo and W. B. Kim, *J. Phys. Chem. C*, 2012, **116**, 18093-18100.
3. J. Joo, T. Uchida, A. Cuesta, M. T. Koper and M. Osawa, *J. Am. Chem. Soc.*, 2013, **135**, 9991-9994.
4. M. Fayette, J. Nutariya, N. Vasiljevic and N. Dimitrov, *ACS Catal.*, 2013, **3**, 1709-1718.
5. C. Du, M. Chen, W. Wang, Q. Tan, K. Xiong and G. Yin, *J. Power Sources*, 2013, **240**, 630-635.
6. Q.-S. Chen, Z.-Y. Zhou, F. J. Vidal-Iglesias, J. Solla-Gullón, J. M. Feliu and S.-G. Sun, *J. Am. Chem. Soc.*, 2011, **133**, 12930-12933.
7. Y.-Y. Yang and S.-G. Sun, *J. Phys. Chem. B*, 2002, **106**, 12499-12507.
8. B. Peng, H.-F. Wang, Z.-P. Liu and W.-B. Cai, *J. Phys. Chem. C*, 2010, **114**, 3102-3107.
9. F. J. Vidal-Iglesias, J. Solla-Gullon, E. Herrero, A. Aldaz and J. M. Feliu, *Angew. Chem. Int. Edit.*, 2010, **49**, 6998-7001.
10. J. V. Perales-Rondón, A. Ferre-Vilaplana, J. M. Feliu and E. Herrero, *J. Am. Chem. Soc.*, 2014, **136**, 13110-13113.
11.Y. Kang, L. Qi, M. Li, R. E. Diaz, D. Su, R. R. Adzic, E. Stach, J. Li and C. B. Murray, *ACS nano*, 2012, **6**, 2818-2825.
12. X. Ge, X. Yan, R. Wang, F. Tian and Y. Ding, *J. Phys. Chem. C*, 2009, **113**, 7379-7384.
13. H. Zhao, C. Yu, H. You, S. Yang, Y. Guo, B. Ding and X. Song, *J. Mater. Chem.*, 2012, **22**, 4780-4789.
14. D. Chen, Y. Zhao, Y. Fan, X. Peng, X. Wang and J. Tian, *J. Mater. Chem. A*, 2013, **1**, 13227-13232.
15. Z. L. Liu, B. Guo, S. W. Tay, L. Hong and X. H. Zhang, *J. Power Sources*, 2008, **184**, 16-22.
16. W.-H. Yang, H.-H. Wang, D.-H. Chen, Z.-Y. Zhou and S.-G. Sun, *Phys. Chem. Chem. Phys.*, 2012, **14**, 16424-16432.
17. G. Saravanan, K. Nanba, G. Kobayashi and F. Matsumoto, *Electrochimica. Acta.*, 2013, **99**, 15-21.
18. R. Iyyamperumal, L. Zhang, G. Henkelman and R. M. Crooks, *J. Am. Chem. Soc.*, 2013, **135**, 5521-5524.
19. C. Venkateswara Rao, C. R. Cabrera and Y. Ishikawa, *J. Phys. Chem. C*, 2011, **115**, 21963-21970.
20. Z. Peng, H. You and H. Yang, *Adv. Func. Mater.*, 2010, **20**, 3734-3741.
21. Y. Xu, S. Hou, Y. Liu, Y. Zhang, H. Wang and B. Zhang, *Chem. Commun.*, 2012, **48**, 2665-2667.
22. S. Yang and H. Lee, *ACS Catal.*, 2013, **3**, 437-443.
23. S. Zhang, Y. Y. Shao, G. P. Yin and Y. H. Lin, *Angew. Chem. Int. Edit.*, 2010, **49**, 2211-2214.
24. Y. Jiang, Y. Jia, J. Zhang, L. Zhang, H. Huang, Z. Xie and L. Zheng, *Chem. Eur. J.*, 2013, **19**, 3119-3124.
25. X. Ge, L. Chen, J. Kang, T. Fujita, A. Hirata, W. Zhang, J. Jiang and M. Chen, *Adv. Func. Mater.*, 2013, **23**, 4156-4162.
26. J. Zhang, H. Yang, B. Martens, Z. Luo, D. Xu, Y. Wang, S. Zou and J. Fang, *Chem. Sci.*, 2012, **3**, 3302-3306.
27. F. Nosheen, Z. C. Zhang, J. Zhuang and X. Wang, *Nanoscale*, 2013, **5**, 3660-3663.
28. D. Xu, S. Bliznakov, Z. P. Liu, J. Y. Fang and N. Dimitrov, *Angew. Chem. Int. Edit.*, 2010, **49**, 1282-1285.
29. Y. Xu, Y. Yuan, A. Ma, X. Wu, Y. Liu and B. Zhang, *Chemphyschem*, 2012, **13**, 2601-2609.
30. Y. Kang and C. B. Murray, *J. Am. Chem. Soc.*, 2010, **132**, 7568-7569.
31. S. Y. Uhm, S. T. Chung and J. Y. Lee, *Electrochem. Commun.* 2007, **9**, 2027-2031.
32. X. Zhao, J. Zhu, W. Cai, M. Xiao, L. Liang, C. Liu and W. Xing, *RSC Adv.*, 2013, **3**, 1763-1767.
33. Y. Huang, S. Zheng, X. Lin, L. Su and Y. Guo, *Electrochimica. Acta.*, 2012, **63**, 346-353.
34. Y. W. Lee, B. Y. Kim, K. H. Lee, W. J. Song, G. Z. Cao and K. W. Park, *Int. J. Electrochem. Sci.*, 2013, **8**, 2305-2312.
35. Z.-C. Zhang, J.-F. Hui, Z.-G. Guo, Q.-Y. Yu, B. Xu, X. Zhang, Z.-C. Liu, C.-M. Xu, J.-S. Gao and X. Wang, *Nanoscale*, 2012, 4, 2633-2639.
36. X. Chen, B. Su, G. Wu, C. J. Yang, Z. Zhuang, X. Wang and X. Chen, *J. Mater. Chem.*, 2012, **22**, 11284-11289.
37. M. Gong, G. Fu, Y. Chen, Y. Tang and T. Lu, *Acs Appl. Mater. Interfaces*, 2014, **6**, 7301-7308.
38. G. Fu, K. Wu, J. Lin, Y. Tang, Y. Chen, Y. Zhou and T. Lu, *J. Phys. Chem. C*, 2013, **117**, 9826-9834.
39. B. Lim, M. Jiang, P. H. Camargo, E. C. Cho, J. Tao, X. Lu, Y. Zhu and Y. Xia, *Science*, 2009, **324**, 1302-1305.
40. L. Ma, C. Wang, M. Gong, L. Liao, R. Long, J. Wang, D. Wu, W. Zhong, M. J. Kim and Y. Chen, *ACS nano*, 2012, **6**, 9797-9806.
41. S. Mourdikoudis, M. Chirea, T. Altantzis, I. Pastoriza-Santos, J. Perez-Juste, F. Silva, S. Bals and L. M. Liz-Marzan, *Nanoscale*, 2013, **5**, 4776-4784.
42. B. Lim and Y. Xia, *Angew. Chem. Int. Edit.*, 2011, **50**, 76-85.
43. J. Moulder, W. Stickle, P. Sobol and K. Bomben,. Handbook of X-ray Photoelectron Spectroscopy, Perkin-Elmer Corporation, Physical Electronics Division: Eden Prairie, MN, 1992.
44. G. Fu, K. Wu, J. Lin, Y. Tang, Y. Chen, Y. Zhou and T. Lu, *J. Phys. Chem. C*, 2013, **117**, 9826-9834.
45. G. Fu, Z. Liu, Y. Chen, J. Lin, Y. Tang and T. Lu, *Nano Res.*, 2014, **7**, 1205-1214.
46. G. Fu, K. Wu, X. Jiang, L. Tao, Y. Chen, J. Lin, Y. Zhou, S. Wei, Y. Tang, T. Lu and X. Xia, *Phys. Chem. Chem. Phys.*, 2013, **15**, 3793-3802.
47. Z. Niu, D. Wang, R. Yu, Q. Peng and Y. Li, *Chem. Sci.*, 2012, **3**, 1925-1929.
48. X. Liu, G. Fu, Y. Chen, Y. Tang, P. She and T. Lu, *Chem. Eur. J.*, 2014, **20**, 585-590.
49. S. Patra, B. Viswanath, K. Barai, N. Ravishankar and N. Munichandraiah, *Acs Appl. Mater. Interfaces*, 2010, **2**, 2965-2969.
50. E. Leiva, T. Iwasita, E. Herrero and J. M. Feliu, *Langmuir*, 1997, **13**, 6287-6293.
51. D. J. Chen, Z. Y. Zhou, Q. Wang, D. M. Xiang, N. Tian and S. G. Sun, *Chem. Commun.*, 2010, **46**, 4252-4254.
52. Z. Cui, M. Yang and F. J. DiSalvo, *ACS nano*, 2014, 8, 6106-6113